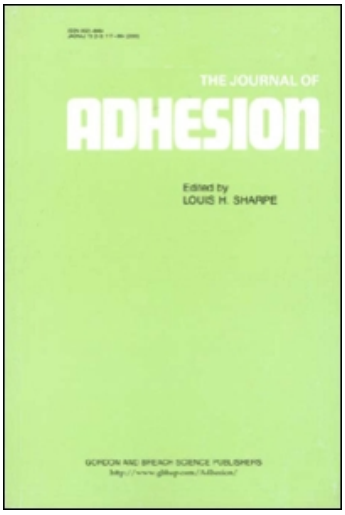

The Journal of Adhesion
Publication details, including instructions for authors and subscription information:
http://www.informaworld.com/smpp/title~content=t713453635

The Influence of Adherend Topography on the Fracture Toughness of Aluminium-Epoxy Adhesive Joints in Humid Environments

A. N. Rider[a]; D. R. Arnott[a]
[a] DSTO Aeronautical and Maritime Research Laboratory, Victoria, Australia

To cite this Article Rider, A. N. and Arnott, D. R.(2001) 'The Influence of Adherend Topography on the Fracture Toughness of Aluminium-Epoxy Adhesive Joints in Humid Environments', The Journal of Adhesion, 75: 2, 203 — 228
To link to this Article: DOI: 10.1080/00218460108029601
URL: http://dx.doi.org/10.1080/00218460108029601

J. Adhesion, 2001, Vol. 75, pp. 203–228
Reprints available directly from the publisher
Photocopying permitted by license only

The Influence of Adherend Topography on the Fracture Toughness of Aluminium-Epoxy Adhesive Joints in Humid Environments

A. N. RIDER* and D. R. ARNOTT

DSTO Aeronautical and Maritime Research Laboratory, GPO Box 4331 Melbourne, Victoria, Australia, 3001

(Received 28 June 1999; In final form 28 July 2000)

The adherend surface topography has a dramatic effect on the durability of structural bonds formed between aluminium and an epoxy adhesive. Systematic changes in the micro-roughness of an aluminium adherend were achieved using an ultra-milling technique to prepare surfaces with topographies ranging from ultra-flat to a sawtooth profile with a base angle of approximately 60° and a peak-to-valley depth of 10 μm. The fracture toughness of double-cantilever beam specimens, stressed in the Mode I direction and exposed to a humid environment was found to change by a factor of approximately one hundred as the sawtooth profile angle was increased. These changes in fracture toughness may be accounted for through complex interrelationships between moisture diffusion and interphase mechanical properties, each with a strong dependence on the surface micro-topography.

Keywords: Surface roughness; Fracture toughness; Bond durability; Aluminium; Epoxy adhesive

1. INTRODUCTION

The performance of a structural adhesive bond depends on a range of interconnected physical and chemical properties of the adhesive and the adherend. No one universal theory is currently capable of

*Corresponding author. Tel.: 61 3 9626 7393, Fax: 61 3 9626 7087, e-mail: andrew.rider@dsto.defence.gov.au

comprehensively describing the mechanical behaviour of an adhesive bond. At the interface, interatomic and intermolecular interactions between the resin and the substrate are fundamental to the formation and maintenance of a structural adhesive bond. Calculations reported in the literature indicate that dispersion and polar forces are sufficient to describe the observed strengths of structural adhesive bonds [1].

The roughness of the adherend also has an influence on the mechanical performance of an adhesive bond [2–16]. Most of these experiments [2–14] were conducted under dry conditions where fracture either occurred or is expected to occur within the adhesive. Mechanisms used to account for the changes in mechanical performance with adherend surface roughness range from mechanical keying or interlocking of the adhesive with the roughened substrate [2–4] to roughness induced changes in the energy dissipation process during fracture [8–11].

Several workers have shown that an abrasion pre-treatment improves the durability of aluminium epoxy joints relative to that of a degreased surface [15, 16]. However, these experiments do not separate the relative influence of physical roughening and contamination effects on joint durability.

This paper examines changes in the energy necessary to fracture an adhesive bond under humid conditions as the micro-roughness of the adherend surface is systematically changed. The surfaces of the aluminium adherends were prepared using an ultra-milling technique to produce carefully controlled surface profiles whilst minimising the secondary influence of variations in surface contaminant and surface chemistry introduced by alternative surface preparation procedures. The physical and chemical properties of the adherend surfaces were carefully characterised. The mechanical measurements were conducted in a hot humid environment under slow crack growth conditions where fracture is expected at the interface between the adhesive and the adherend [17]. An examination of energy dissipation in the equilibrium fracture process under humid conditions is conducted, using concepts adapted from the theories of Carré [18] and Cognard [19]. The fracture surfaces were carefully characterised using surface analytical techniques to establish the locus of failure.

2. ENERGY DISSIPATION AND FRACTURE MECHANICS

A bonded double-cantilever beam, stressed in Mode 1 opening, is widely used to assess the environmental durability of an adhesive bond [20]. Crack growth data can be used to calculate the energy delivered from the stressed cantilevers to generate a freshly-cracked surface. The elastic energy release rate, G_1, can be calculated using Eq. (1) [21].

$$G_1 = \frac{Ed^2h^3}{16} \frac{[3(a+0.6h)^2 + h^2]}{[(a+0.6)^3 + ah^2]^2} \tag{1}$$

where h is the thickness of the aluminium adherend, E is Young's modulus, d is the displacement of the adherends by the wedge and a is the crack length from the bearing edges of the wedge to the crack-tip. The h^2 and ah^2 terms allow for the shear contribution to the elastic energy and the $0.6h$ term is a correction for adherend rotation [21].

For a simple double-cantilever beam bonded specimen, the calculated elastic energy release rate, G_1, decreases with the inverse fourth power of crack length. As the crack extends, the crack velocity slows, the stress in the cracking region decreases and G_1 approaches an equilibrium value. Under humid conditions, it is common for the fracture to occur at the interface between the adhesive and the adherend [17] and G_1 tends toward a new equilibrium G_{1SCC} [22]. This G_{1SCC} represents fracture in a bond fully degraded by the moisture present just ahead of the crack-tip [22].

Some authors have proposed that the energy dissipated in the fracture of an adhesive bond, G_C, can be written as:

$$G_C = G_i(1+f) \tag{2}$$

where, G_i is an intrinsic fracture energy and f is a factor that considers visco-elastic and plastic energy dissipation as a multiple of G_i [23]. In those fractures where failure occurs within the adhesive, plastic deformation processes are considered to be the predominant energy dissipation mechanism [24]. A roughened surface may influence adhesive plastic deformation processes and the fracture toughness of adhesive bonds [8–11, 13, 14].

Alternative approaches to fracture in plasticised or rubbery materials have also been developed. Cognard [19] has described a molecular-scale, load-sharing mechanism to relate the fundamental work of adhesion, W_A, to the measured fracture energy for a wide range of adhesive-adherend joints tested using wedge-style experiments. Cognard adapted the theory of Carré [18] for cross-linked hot melt and rubber-toughened epoxy systems. At zero crack velocity, the fracture energy, G_0, is described in Eq. (3):

$$G_0 = (N \cdot U)W_A \tag{3}$$

where N and U combine to form an energy dissipation term. N represents the effective number of links each aluminium-to-epoxy bond makes by being bonded to the cross-linked polymer network. N can also be referred to as the number of stress-sharing networks. U is the ratio of the bond energy of the aluminium – epoxy bond to the energy of molecular links within the resin. Practically, U approximates to unity. W_A is an approximation and was used to provide an estimate of the linkage density between the surface and the adhesive. The value used in calculations is based on reported literature estimates [18, 19], which are unable to resolve the nature of the bonding between the epoxy and metal surface, *i.e.*, covalent, polar, *etc.* The nature of the bonding interaction is not critical to the calculation, given that dispersion forces have been indicated to be more than sufficient to produce the bond strength observed for many practical adhesive systems [1]. In terms of displacement of adhesive bonds from metallic substrates, humidity has often been reported to displace surface molecules in which polar or covalent bonding is believed to be present [17] and the generality of Eq. (3) to humid fracture appears reasonable. Cognard demonstrated that the fracture energy for cohesive fracture within the adhesive was sensitive to surface treatment, which provided some support to the generality of the theory to both interfacial and cohesive fracture processes in adhesive bonds [19].

In this paper, the possibility of energy dissipation by both plastic-dissipation processes and stress-sharing networks is considered. An energy term, Y, to describe plastic dissipation processes, is added to the Cognard expression as described in Eq. (4):

$$G_C = (N \cdot U)W_A + Y \tag{4}$$

A general approach used previously [23] enables the energy dissipated to be expressed as:

$$G_C = (N \cdot U) \cdot W_A \cdot \{1 + F\} \tag{5}$$

where F is a factor, without units, to describe the relative magnitude of energy dissipated through plastic-deformation processes to energy dissipated through the stress-sharing mechanism. For the specific case of humid fracture under Mode 1 opening, examined in this paper, G_C becomes G_{1SCC}.

3. EXPERIMENTAL

3.1. Surface Characterisation

X-ray photoelectron spectroscopy (XPS) was performed using a Kratos model XSAM-800 spectrometer. Spectra were recorded using MgK_α radiation, with the spectrometer operating in Fixed Retard Ratio (FRR) mode with a ratio of 24 for low-resolution scans and 53 for high-resolution scans. The area of analysis in the high-magnification mode of operation was approximately 2 mm in diameter. All spectra were calibrated relative to adventitious carbon at 285.0 eV and quantified using the sensitivity factors derived from polymeric and metal oxide reference materials.

Atomic Force Microscopy (AFM) measurements used a Park Scientific Auto Probe LS model AFM in constant force mode. The scanning probe was calibrated using a grid of known dimensions. All images were corrected using a second-order polynomial background subtraction to compensate for thermal variations, piezoelectric hysteresis and sample tilt. The pyramidal silicon nitride micro-lever tip had an angle of 55° relative to the surface plane.

Contact angle (θ) measurements of a 50 µl drop of 20 MΩcm deionised water were conducted on aluminium surfaces immersed in AR grade hexane, octane or hexadecane. A digital image of the drop was analysed with image processing software.

3.2. Aluminium Surface Pre-treatments

Clad 2024 T3 aluminium alloy adherends, cut from 3.2 mm-thick sheet, were degreased and surface prepared with either an ultra-milling or a grit-blast process. The ultra-milled surfaces were prepared using a Cambridge Instruments attachment to a Jung Polycut E microtome. The ultra-milling process was conducted with specially manufactured milling blades to produce three sawtooth profiles. The 40 mm milling radius produced a groove direction perpendicular to the sample length [25]. An automated grit-blast treatment was also conducted using 50 μm alumina particles delivered with an impact density of 1.2 g cm^{-2} [26]. The 100 μm-thick clad layer on the aluminium alloy remained on both the ultra-milled and the grit-blast prepared surfaces.

3.3. Bond Preparation and Fracture Analysis

The adherends were bonded with Cytec® FM-73 epoxy film adhesive and cured at 120°C for 1 hour in a platen press. The adhesion durability was assessed in 95% relative humidity at 50°C using the method prescribed in ASTM D3762-79 [27]. A 1.5 mm wedge was inserted in a double-cantilever beam specimen and the crack growth was monitored as a function of time.

XPS analysis of failed wedge specimens was conducted at a position as close to the crack tip region as possible. Scanning Auger Microscopy (SAM) analysis of a metal failure surface employed a 10 kV electron beam with 2 μm spot resolution to map the spatial distribution of aluminium in the metallic state using the Al KLL Auger transition at 1392.9 eV. Topographic correction of the intensity distribution involved dividing the peak minus background map by the background map.

Secondary electron microscopy (SEM) was performed on cross sections of the bondline from intact wedge specimens. Micrographs were acquired behind, near and in advance of the crack front. The edge of the wedge samples were metallographically polished prior to wedge insertion and gold coated after removal from the extended exposure in the humid environment, prior to the SEM analysis.

4. RESULTS

4.1. Surface Topography

The ultra-milling process generates sawtooth profiles on the aluminium alloy adherend surface. Figure 1 shows a SEM cross-section of the aluminium-to-epoxy adhesive bond and illustrates a saw-tooth profile generated on the adherend by the 60° ultra-milling blade. The peak-to-valley depth of the saw-tooth is approximately 10 μm and the base angle, A, is approximately 60°. The base angle is defined in the accompanying sketch in Figure 1. The complementary surface

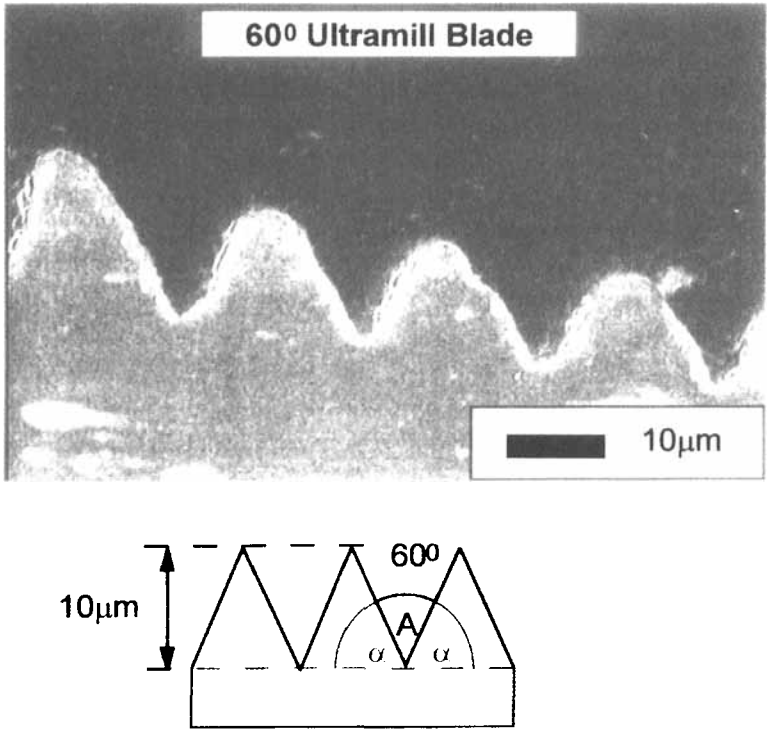

FIGURE 1 SEM cross-section of the 60° ultramilled aluminium bonded to epoxy resin. Also indicated is a diagrammatic representation of the ultramill profile showing the base angle.

profile angle, α, which is related to the base angle through $\alpha = (180 - A)/2$, is also defined in the sketch.

Figure 2 provides three-dimensional AFM images of a grit-blasted and an ultra-milled aluminium surface with a base angle of 180°. The 180° surface has 50 nm steps and surface relief of less than 5 nm, which suggests there is no evidence of features capable of substantial mechanical interlocking with the adhesive. The grit-blast surface has topographical features of approximately 2 μm in height with varying angles. The line profiles taken from the AFM image indicated features with surface profile angles approaching 45°. These translate to equivalent base angles of approximately 90°.

4.2. Surface Chemistry

Table I indicates the relative atomic composition obtained from XPS spectra of the 180° ultra-milled and grit-blasted aluminium surfaces. The oxide thickness was estimated to be approximately 2 nm for the 180° ultra-milled surface [28, 29]. Since the ultra-milled surfaces were each prepared by a similar method, the chemistry of the three surfaces is expected to be similar. In comparison, the grit-blasted surface appears to have a thicker oxide and a higher hydrocarbon contaminant concentration than the ultra-milled surface. The surface roughness of the grit-blast surface will enhance the surface signal measured by XPS and, therefore, the apparent oxide and contaminant layer thickness relative to that of the flat 180° ultra-milled surface. After corrections for surface roughness effects are made, the oxide thickness was estimated to be 3 nm with the carbon contaminant thickness almost double that of the flat 180° ultra-milled surface.

The surface energy of the 180° ultra-milled aluminium surface was estimated using the method of Carré and Schultz [30]. The dispersion, γ_S^D, and polar, γ_S^P, surface energies were calculated using Eq. (6) [30]:

$$\gamma_L - \gamma_H + \gamma_{LH}\cos\theta = 2\left((\gamma_L^D)^{1/2} - (\gamma_H)^{1/2}\right) \cdot (\gamma_S^D)^{1/2} - 2(\gamma_S^P \cdot \gamma_L^P)^{1/2} \tag{6}$$

where γ_H is the surface tension of the hydrocarbon in air, γ_{LH} is the interfacial surface tension between the water and hydrocarbon and γ_L

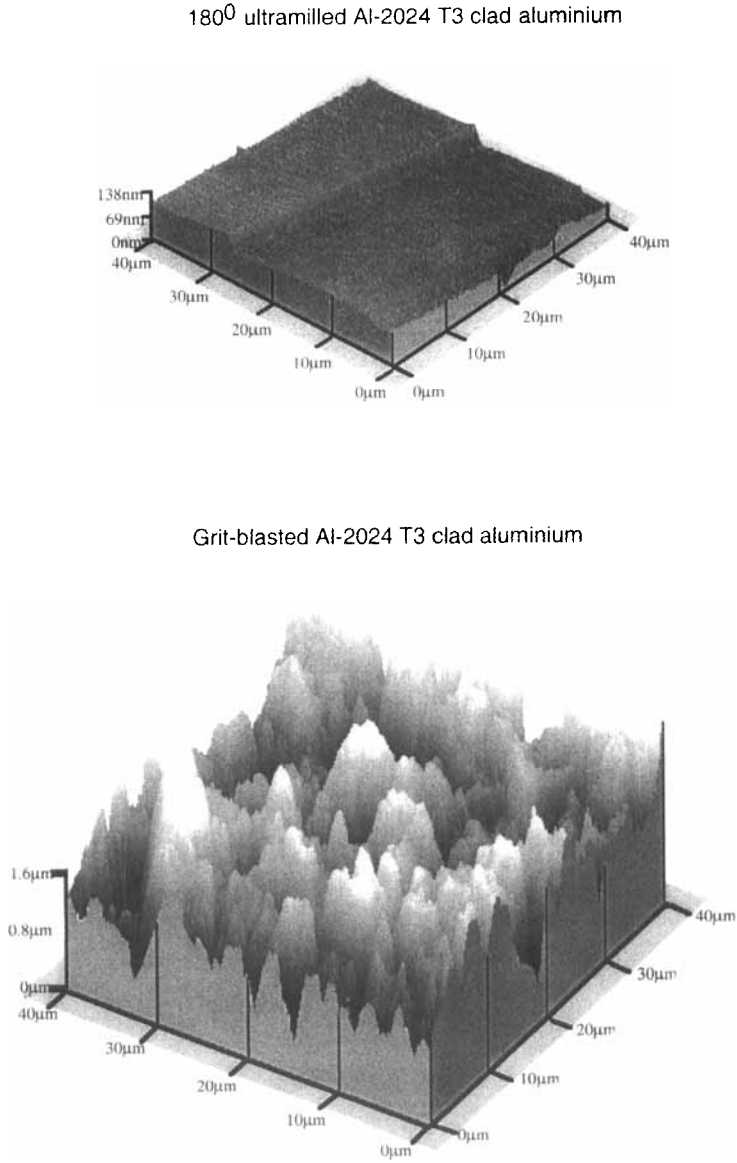

FIGURE 2 3-D AFM images of 180° ultramilled and grit-blasted aluminium surfaces.

TABLE I Surface atomic composition of 180° ultramilled and grit-blasted aluminium

	Atomic composition (%)			
Treatment	*O1s*	*C1s*	*A12p metal*	*A12p oxide*
Ultramilled (180°)	45.3	7.1	23.0	24.6
Grit-Blast	55.3	12.1	6.0	26.6

TABLE II Surface and interfacial energies of water and alkanes used [30]

Alkanes	γ_H (mJm^{-2})	γ_{LH} (mJm^{-2})	*Water* (mJm^{-2})
Hexane	18.4	51.1	$\gamma_L = 72.6$
Octane	21.3	51.0	$\gamma_L^D = 21.6$
Hexadecane	27.1	51.3	$\gamma_L^P = 51.0$

is the surface tension of water. The superscripts D and P refer to the dispersion and polar component of the surface tension value being used. (The surface tension values used in the calculations are provided in Tab. II [30].)

The plot in Figure 3 was used to calculate γ_S^D and γ_S^P from the intercept and gradient, respectively. The linear fit in Figure 3 for the 180° ultra-milled aluminium had a correlation coefficient greater than 0.99. The calculated polar and dispersion energies were 41 mJm^{-2} and 142 mJm^{-2}, respectively. Based on a maximum and minimum gradient and the scatter in measured contact angle values, the approximate percentage error in γ_S^D is 20% and γ_S^P is 5%.

4.3. Fracture Toughness in Humid Environments

Figure 4 shows the crack length as a function of exposure time (compressed using square root of time presentation) to a humid environment for the wedge specimens manufactured using adherends prepared with the ultra-milling blades and the grit-blast treatment. Initially, the crack length increases rapidly under the influence of high stress and the degrading environment. After approximately 50 hours the crack velocity decreased as the crack length increased and the driving stress decreased. After approximately 150 hours the crack length for all surface profiles had approached an equilibrium value. In

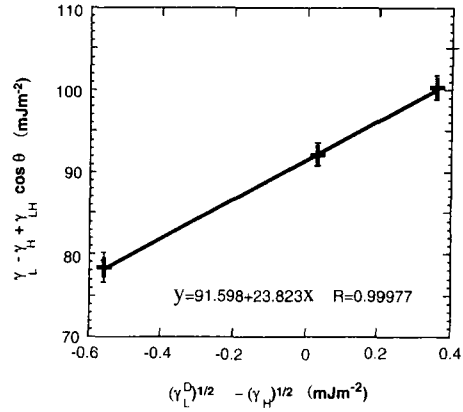

FIGURE 3 The surface energy plot of 180° ultramilled aluminium. Error bars represent the standard deviation for at least six separate measurements.

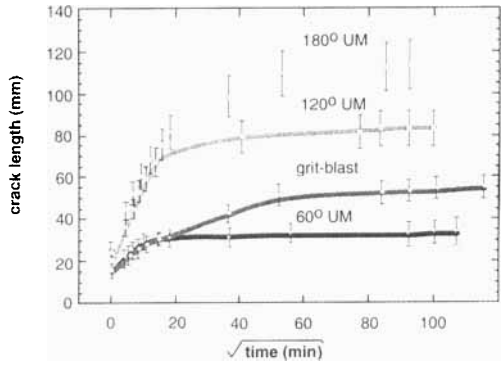

FIGURE 4 Crack length as a function of humid exposure time for epoxy-aluminium wedge samples showing the effect of ultramill base angle. Error bars represent the standard deviation of triplicate samples.

the present paper, this equilibrium crack length was evaluated at a crack velocity of 1×10^{-4} mm s^{-1}. After the wedge samples had been fully tested and separated, they were examined on a flat surface. Plastic deformation of the adherends was negligible.

The crack growth data can be used to calculate the energy delivered from the stressed cantilevers to generate a freshly cracked surface as described in Eq. (1). The value of E was 72 GPa. Since the wedge-test

measurements were conducted in a humid environment, values of G_1 calculated from final crack lengths (evaluated at a crack velocity of 1×10^{-4} mm s^{-1}) in Figure 5, represent G_{1SCC}. Values of G_{1SCC} for each of the ultra-milled specimens and the grit-blasted specimen are presented as a function of tan α in Figure 5, where α is defined in Figure 1. Error bars were calculated using error estimates for the crack-length measurements, wedge thickness and adherend thickness. G_1 is inversely proportional to a^4 and the error decreases as G_1 approaches G_{1SCC}.

As plastic deformation of the adherends can lead to concern for the validity of fracture mechanics calculations, checks were conducted to validate the values of G_{1SCC}. Independent measurements using bolt-loaded 12.8 mm thick adherend specimens manufactured from Al–2024 T3 aluminium alloy, with a similar grit-blast surface treatment, the same FM-73 adhesive and tested in the same environment of 50°C/95%R.H., yielded a G_{1SCC} value of 100 Jm^{-2} [31, 32]. This is similar to the value of 96 Jm^{-2} measured for the grit-blast specimen as shown in Figure 5. A yield stress calculation [21] indicates that the 3.2 mm thick Al-2024 T3 aluminium alloy adherends are just at the threshold of plastic deformation when tested with FM-73 adhesive ($G_{1C} = 2$ kJm^{-2} [33, 34]) under dry conditions and is well below this threshold when the adhesive bond is degraded by moisture. The use of a thin 1.5 mm wedge, inserted slowly in a press, also decreases the initial cantilever

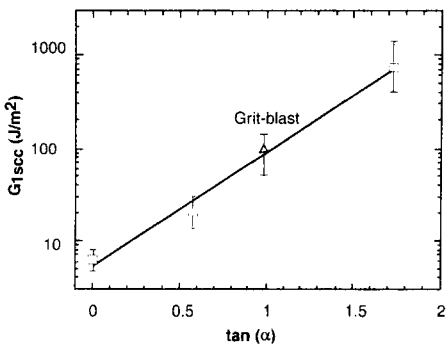

FIGURE 5 G_{1SCC} determined from crack-length data at 150 hours in Figure 4 as a function of the resolved vertical and horizontal component of the surface profile angle. The error bars show error associated with the standard error in crack length in Figure 4 and errors in adherend and wedge thickness.

impulse stress over that of the standard 3.2 mm wedge. The combined evidence indicates that the calculations of G_{ISCC} are valid in the present series of experiments.

4.4. SEM Cross-sectional Analysis of Wedge Specimens Exposed to 50°C/100% R.H.

Figure 6 shows a cross-sectional micrograph of the bondline from a 60° ultra-milled wedge sample. The image provides details of the epoxy resin fracture surface in the region that corresponds to crack growth in a dry environment, resulting in cohesive fracture within the adhesive near the interface. The image is characterised by furrows running in the direction of crack propagation and the presence of voids. These features are consistent with plastic deformation processes associated with dry fracture reported in the literature [24].

Figure 7 also shows a cross-sectional SEM micrograph taken from the bondline of a 60° ultra-milled wedge sample. The image of the epoxy resin fracture surface was acquired a few millimetres behind the crack-tip and corresponds to a region where visual inspection of the complementary fracture surfaces suggested failure was interfacial.

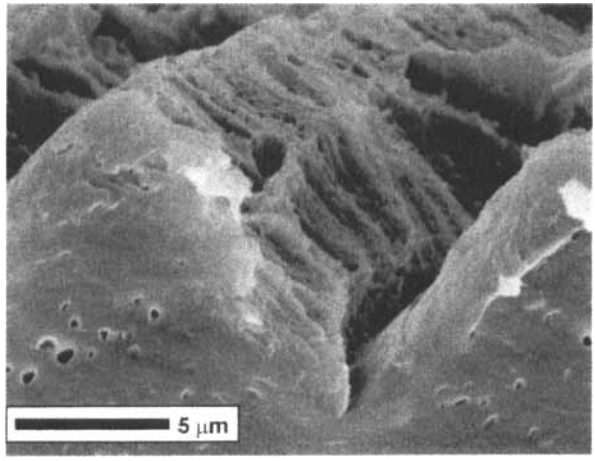

FIGURE 6 SEM image taken of the 60° ultramill wedge failure surfaces showing features consistent with cohesive failure within the adhesive. The experiment was conducted under dry conditions.

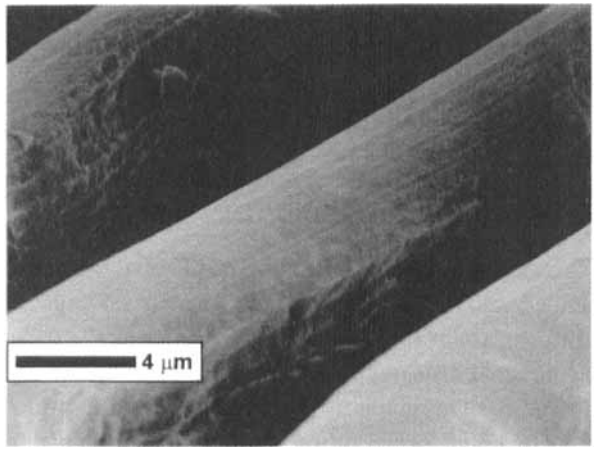

FIGURE 7 SEM image taken of the adhesive face of the 60° ultramill wedge failure surface showing features at the adhesive-metal interface. The observation was made near the crack-tip and the experiment was conducted under humid conditions.

The failure surface of the adhesive contrasts with that observed in Figure 6. The adhesive fracture face shows a smooth surface with fine lines running in the milling direction. There does not appear to be significant evidence of the cavities or furrows observed in the dry fracture micrographs, shown in Figure 6.

Figure 8 shows a cross-sectional SEM micrograph of the 60° ultra-mill wedge sample, taken at an oblique angle. The image shows the interface between the aluminium and epoxy resin a few millimetres ahead of the crack-tip. The lower magnification image shows large interfacial cavities or voids in the peak and valley region between the metal and adhesive interface. The higher magnification image in the bottom right hand corner indicates an adhesive bridge or link between the adhesive and aluminium in the centre of the large interfacial cavity or void. The image in the top right corner highlights a smaller void or cavity of approximately 1 μm in length.

Figure 9 shows the interfacial region of the 60° ultra-milled wedge sample several millimetres ahead of the crack-front. The image indicates that the interface between the aluminium and adhesive is not as well defined as in Figure 8 and suggests fewer interfacial voids or cavities are present in this relatively unstressed region.

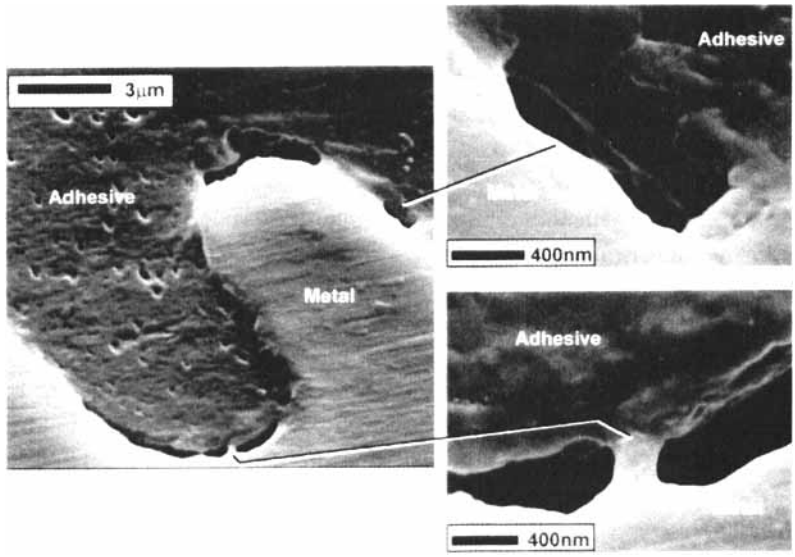

FIGURE 8 SEM images taken of the metal-to-adhesive interface slightly in advance of the crack-tip for the 60° ultramill wedge sample, indicating the presence of interfacial voids or micro-cavities.

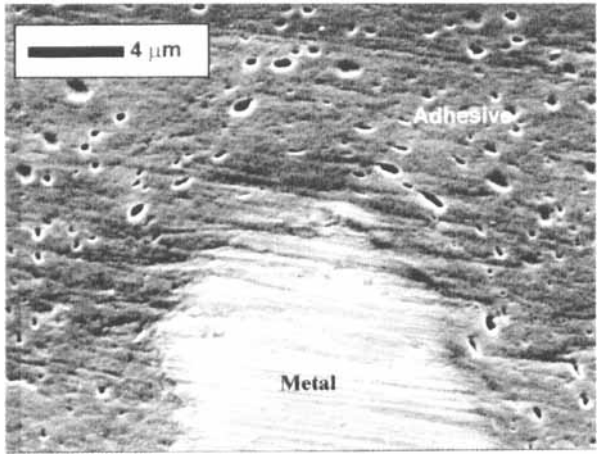

FIGURE 9 SEM image taken of the metal-to-adhesive interface for the 60° ultramill wedge sample in advance of the crack-tip, corresponding to a relatively unstressed, undegraded region.

4.5. Failure Surface Analysis

Table III shows the results of the XPS analysis of the failure surfaces resulting from the humid fracture of the ultra-milled and grit-blasted aluminium-epoxy joints. The "adhesive" side represents the failure surface with the epoxy resin appearance and the "metal" side, the failure surface with the aluminium appearance. The fracture analysis indicates that failure for all three ultra-mill samples is predominantly at the interface between the epoxy resin and the aluminium. The carbon level on the "adhesive face" is over 70 atom per cent, whereas on the "metal face" it is less than 10 atom per cent when corrected for approximately 20% carbon typical of adventitious adsorption on the "metal" face [28]. This suggests that the residual adhesive on the "metal face" is thin and unlikely to be uniformly distributed. The two or three atom per cent of oxidised aluminium on the "adhesive face" is insufficient for fracture in a weakened oxide to be the principal mode of failure for the ultra-milled specimens. The progressive increase in *N* 1s concentration on the "metal faces" of the ultra-milled samples, as the base angle is changed from 180° ultra-flat to 60°, indicates that some epoxy adhesive is retained as the base angle decreases toward 60°. Failure of all three ultra-mill profiles in humid environments either occurs at, or is controlled by, the metal oxide to adhesive interface. The grit-blasted sample, however, indicates a higher level of aluminium on the "adhesive" surface, suggesting that some fracture has propagated in the aluminium oxide layer.

The "metal" failure surface for the specimen with a 180° base angle indicated that the region behind the crack tip, which had been directly

TABLE III XPS analysis of the failed wedge specimens fracture surfaces. Aluminium was pre-treated by ultramilling or grit-blasting

	Failure	*Atomic composition* (%)				
Pre-treatment	*side*	*O1s*	*N1s*	*C1s*	*C12p*	*A12p*
180° ultramilled	metal	46.2	–	28.4	0.6	24.8
180° ultramilled	adhesive	25.7	0.7	69.6	0.3	3.7
120° ultramilled	metal	52.0	0.2	21.1	1.1	25.6
120° ultramilled	adhesive	19.2	2.3	76.1	0.3	2.1
60° ultramilled	metal	48.4	1.3	26.0	–	24.3
60° ultramilled	adhesive	12.3	1.8	85.3	–	0.6
grit-blast	metal	49.5	–	25.9	–	24.6
grit-blast	adhesive	19.2	1.9	75.9	–	9.0

exposed to the moist environment, had a dull appearance. Approximately 5 millimetres ahead of the crack an unoxidised area represented a region of low interfacial strength. The initial wedge opening and the zone of forced opening ahead of the unoxidised section (both conducted at room temperature in dry environments) led to cohesive failure in the adhesive. The ultra-milled specimens with base angles of 120° and 60° showed similar fracture surfaces. The extent of unoxidised surface regions ahead of the crack tip decreased as the surface base angle decreased, as shown in Table IV.

The results of SAM conducted on the metal face of the 180° ultra-milled wedge sample in the region ahead of the crack tip is shown in Figure 10a. These maps were acquired using the aluminium peak in the metallic state. Representative spot spectra were acquired at sites across each map as shown in Figure 10b. These maps and spectra indicated that localised areas of oxidised aluminium, thicker than the 10 nm

TABLE IV Length of degraded region ahead of crack tip as a function of adherend profile base angle

Adherend profile base angle	180°	120°	60°
Length of degraded region (mm)	5	1	< 0.5

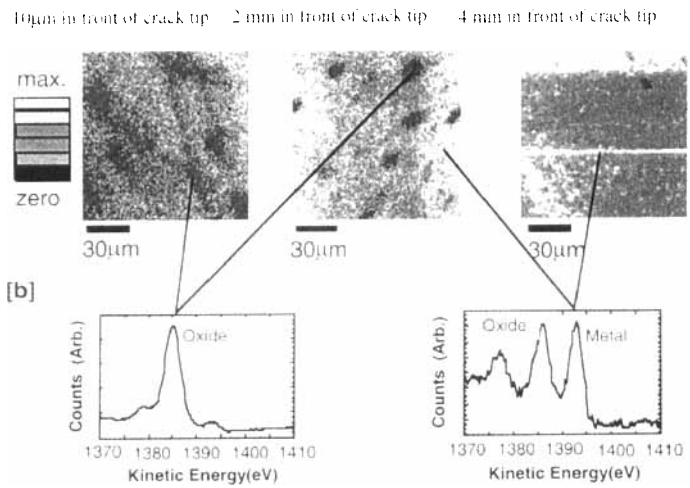

FIGURE 10 (a) SAM maps indicating the distribution of metallic aluminium at positions near the crack-tip area; (b) SAM spectra acquired at the points indicated.

escape depth of the Auger electrons, had developed in the region ahead of the crack tip. The density of these localised oxidised areas decreased as the distance ahead of the crack tip increased.

Auger spectra taken in the dull region behind the crack (not shown) indicated that only oxidised aluminium was present. The oxide here was thicker than the 10 nm escape depth of the Auger electrons due to extended direct exposure to the humid atmosphere.

5. DISCUSSION

5.1. Ultra-milled Surfaces – Surface Topography and Chemical Character

The best improvements in adhesive bond durability performance can be achieved with chemical treatments, anodisation or coupling agents. Although the literature indicates that both surface chemistry and surface topography play a role in bond performance, the relative influence of chemical interactions and surface topography is not easily separated. Work by Critchlow and Brewis indicates that abrasion with finer grits can improve bond durability [35]. However, these experiments do not characterise the surface in sufficient detail to establish principles underpinning the role of changes in surface roughness on bond durability. Our research shows that contamination of an abraded or grit-blasted adherend prior to bonding strongly affects bond durability [17]. It is, therefore, very important to ensure that the chemical state of roughened surfaces is invariant during studies of the effects of surface roughness on bond durability.

The ultra-milling method varies the surface profile whilst minimising the secondary influence of variations in surface contaminants and surface chemistry introduced by solvent-based cleaning or chemical etching approaches. The low contaminant levels for the ultra-milled surfaces relative to that for the grit-blasted surface are described in Table I. The surface energy of $183\,mJm^{-2}$ for the 180° ultra-milled surface, as described in Section 4.2, is similar to values reported by Carré and Schultz [30] for anodised aluminium and Mantel and Wightman [36] for plasma-cleaned steel. This surface energy is consistent with optimal characteristics for bonding with an epoxy

resin and provides confidence in the ultra-milling technique as a method of varying surface topography with minimal variations in chemical behaviour.

The paper has practical relevance to the durability performance of loaded toughened-epoxy joints where interfacial failures are frequently observed, particularly in cases where the surface treatment is mediocre.

5.2. G_{1SCC} as a Function of Surface Profile

The ultra-milled surface profile has a dramatic influence on the ease of humid fracture of a structural adhesive bond under Mode 1 opening (see Fig. 4) and on the energy G_{1SCC} (see Fig. 5) needed to fracture the adhesive bond. The value of G_{1SCC} for the degraded bond on the rough 60° ultra-milled wedge sample is a factor of approximately 100 greater than that on the ultra-flat 180° sample. To the knowledge of the authors, this effect of surface roughness on bond durability has not been previously observed. This is possibly due to a concentration of durability studies on industrially-roughened surfaces. The grit-blasted surface has a distribution of surface profile angles, with some dominant angles at 45°, whilst the majority of the angle distribution range is less than 30°. The 60° ultra-milled surface profile produces much steeper surface profile angles than those produced by standard abrasion and grit-blast procedures. At the other extreme, the 180° ultra-mill produces a clean, ultra-flat surface (see Fig. 2) not achieved by standard surface preparation methods.

Fracture of the profiled ultra-milled bonded specimens in humid environments appears to occur near the smooth metal interface (see Fig. 7). The surface analysis described in Section 4.5 indicates that the fracture is at the interface between the metal oxide and the epoxy adhesive. This contrasts with the dry fracture case where failure occurs within the adhesive (see Fig. 6). Some contribution to the 100-fold improvement in G_{1SCC} observed in changing the base angle from 180° to 60° can be attributed to the factor of 2 change in surface area and the resultant increase in the number of effective molecular or polar bonds. The absence of obvious surface relief on the ultra-milled surfaces capable of keying with the adhesive, (see Figs. 1 and 2) suggests that mechanical interlocking may not be a dominant

mechanism here. However, the surface profile could also influence the micro-mechanical behaviour of the material at the interface between the adhesive and the adherend and the rate of moisture ingress into the interfacial region, which, in turn, influences the degree of degradation and the micro-mechanical properties of the bond. This complex set of interactions is considered individually in Sections 5.3 to 5.5.

5.3. Interfacial Micro-mechanics

Sargent [12], in studies of chromic acid anodise pre-treatment of aluminium for bonding to epoxy resin, suggested that variations in joint strengths can depend on the angle of adherend surface features. Briscoe and Panesar [14] and Zhang and Spinks [13] used the concept of resolving surface stress on a rough surface into horizontal and vertical components to account for energy-dissipation processes during joint fracture. Although these experiments refer to failure under dry conditions, the concept of describing surface topography in terms of surface angle is adopted in this paper.

The sawtooth surface profile introduces a microscopic surface shear component to the microscopic surface peel component of the flat surface as shown in Figure 11. Here, the microscopic surface shear component is aligned with the Mode 1 opening direction. The ratio, R, of the microscopic surface shear to microscopic surface peel

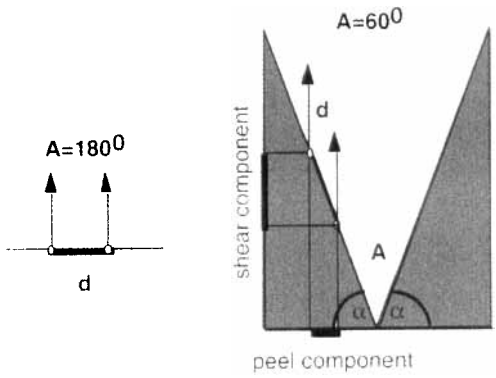

FIGURE 11 The forces on individual bonds at the epoxy-aluminium interface resolved into microscopic surface shear and peel components.

component is defined in Eq. (7):

$$R = \tan(\alpha) = \frac{\text{Microscopic Surface Shear}}{\text{Microscopic Surface Peel}} \tag{7}$$

In simple geometric terms, individual bonds attached to the 180° flat surface will only experience load in the surface peel direction, whereas the 60° base angle will see 1.7 times as many bonds sharing load in the surface shear direction than in the surface peel direction.

The semi-log plot of G_{1SCC} as a function of tan α (or R), shown in Figure 5, suggests that the surface shear component plays an important role in slow interfacial fracture of an adhesive bond in warm humid conditions and indicates a relationship of the form:

$$G_{1SCC} = G_{1SCCf} \cdot \exp(k \cdot R) = G_{1SCCf} \cdot \left[1 + k \cdot R + \sum_{i=2}^{\infty} \frac{(k \cdot R)^i}{i!}\right] \tag{8}$$

where G_{1SCCf} represents G_{1SCC} for the 180° base angle sample and k is the gradient of the plot. This k can be viewed as a sensitivity factor. Here $G_{1SCCf} = 5.9\,\text{Jm}^{-2}$ and $k = 2.9$.

The polynomial expansion, shown in Eq. (8), indicates that G_{1SCC} can be expressed as a sum of a linear term $(1+k \cdot R)$ and a power series term $\sum_{i=2}^{\infty}((k \cdot R)^i/i!)$. This power series term suggests that nonlinear factors, with a strong dependence on the microscopic surface shear component of stress, control the degree of bond degradation at the interface between the adhesive and the metal oxide.

5.4. Influence of Surface Roughness on Energy Dissipation

The energy-dissipation mechanisms responsible for humid fracture do not appear to be as well established in the literature. In the humid environment, the locus of fracture has shifted to the interfacial region (see Section 4.5) and the interface now strongly influences the energy-dissipation processes. Any possibility for the development of a plastic zone will be constrained by the metallic adherend. In addition, saturation of FM 73 adhesive (with a dry glass transition temperature (T_g) of 98°C) by moisture will suppress the T_g by up to 20°C [37–39]. The presence of moisture and the very slow crack growth rates of

1×10^{-4} mm s^{-1} suggest that plasticisation (or development of rubbery characteristics) of the adhesive in the cracking zone may be expected. Arnott and Kindermann [40] have observed this form of plasticisation of a similar adhesive on a macro-scale. Thus, alternative mechanisms to those described for dry fracture, may be expected to contribute also to the relief of stress during the humid fracture process. The fact that G_{1SCC} values in Figure 5 are well below the G_{1C} of 2 kJm^{-2} for Cytec FM 73 adhesive, indicates that Y, and hence F, have decreased substantially from that in the dry fracture case.

Further analysis of Eq. (8) may consider the failure of the specimens manufactured with the 180° ultra-flat adherends. Equation (5) could be rewritten by substituting G_{1SCCf} ($= 5.9$ Jm^{-2}) for G_C and N_f (the number of stress-sharing networks specifically for an ultra-flat 180° surface) for N. Assuming that W_A is approximately 0.2 Jm^{-2} for an aluminium-epoxy bond [19], then as F is decreased toward zero, the maximum value of N_f is of the order of 30. This implies that the range of stress-sharing networks on a fully-degraded, ultra-flat surface would only be a few nanometres. The calculation is consistent with the description of humid fracture being influenced by properties close to the metal-adhesive interface and the influence of energy dissipation though macroscopic plastic deformation processes being negligible.

Humid fracture of adhesive bonds on the roughened adherend surfaces also needs to consider the exponential increase in G_{1SCC} with R described in Eq. (8). For surface profile angles with $\alpha < 18°$, the power series term $\sum_{i=2}^{\infty}((k \cdot R)^i/i!)$ is less than the linear term $(1 + k \cdot R)$, which implies that for relatively flat surfaces the fracture is dominated by relatively short-range microscopic processes and interactions right at the interface. As α increases above 18° the power series term rapidly dominates the energy-dissipation process. The power series term relates to energy-dissipation processes due to the influence of long-range materials properties (*e.g.*, viscoelastic and plastic deformation) and mechanical processes (*e.g.*, roughness-induced stress variations). The roughened surfaces produced by the grit-blast surface treatment fall into the latter category. It is important to emphasise that this analysis refers to the fully-degraded adhesive bond where failure was interfacial, as described in Section 4.5. The longer-range influences in the fracture process, as α increases, are reflected in the fracture surface analyses. This analysis shows

increasing $N1s$ (see Tab. III) and, hence, increasing adhesive on the metal face as the surface profile angle increases toward 60°. The surface analysis, however, shows that humid fracture remains very close to the metal oxide interface.

5.5. Stress-based Water Diffusion and the Influence of Surface Topography

The mechanics of the humid fracture of an adhesive bond described in the previous section considers the influence of surface topography on the nature of energy-dissipation processes. Moisture ingress into a stressed adhesive joint and the influence of surface topography on that process needs to be considered.

The moisture-affected zone for the 180° profile surface is 5 mm (see Tab. IV) under relatively low-stress conditions indicated by a G_{1SCCf} of 5.6 J m^{-2}. By contrast, the moisture-affected zone of the 60° profile case is 0.5 mm (see Tab. IV), under relatively high-stress conditions indicated by G_{1SCC} of 600 J m^{-2} (see Fig. 5). The inverse relationship between the extent of the moisture-affected zone and the stress conditions at the crack tip is not consistent with activation-controlled moisture diffusion under applied stress.

Comyn suggested that enhanced diffusion observed in some loaded composite systems may be due to stress causing microscopic interfacial defects which provide an alternative path for moisture ingress [41, 42]. Other workers have also considered the role of interfacial imperfections in providing sites for moisture ingress [43–45]. Cognard [19] has shown interfacial cavities ahead of the crack front for fractured wedge samples produced from epoxy resin and glass substrates. In the present paper, Figure 8 shows interfacial micro-cavities in the stressed region ahead of the crack tip for the case of bonds manufactured with epoxy adhesive and 60°-profiled aluminium adherends. Figure 10 and Ref. [17] show localised oxidation consistent with moisture diffusion through micro-cavities. This accumulated evidence has led to a Stress Based Diffusion Model of interfacial water diffusion facilitated by stress-induced cavities (or voids) in the adhesive ahead of the crack tip [17, 25, 46].

It is worth speculating how the introduction of micro-roughness could affect this proposed moisture diffusion mechanism.

In the case of the 180° profile wedge sample, microscopic surface peel would dominate the interfacial stress. Discussion in Section 5.4 suggested that energy dissipation processes during humid fracture may be localised in the vicinity of the interface, with the range of co-operative interactions extending only a few nanometres. Under these conditions, a relatively low level of stress could open extended regions of micro-cavities and, thus, facilitate rapid diffusion of moisture some considerable distance ahead of the crack tip. For the surfaces with $\alpha > 18°$, energy dissipation could occur through longer-range cooperative physical processes in the adhesive, such as plastic deformation of the adhesive. As a consequence, the interfacial stress at the adherend-to-adhesive interface could be diminished, leading to a reduction in the size and population of the interfacial micro-cavities, despite the high external stress conditions relative to the 180° wedge sample. In the specimens with higher surface profile angles, the diffusion of moisture ahead of the crack tip is retarded by the roughness-induced properties of the adhesive.

This paper, through separate analysis of the mechanisms of moisture diffusion and energy dissipation processes during fracture, provides some insight into the important properties that need to be examined.

6. CONCLUSIONS

The ultra-milling technique is a convenient way of introducing micro-roughness to metallic adherends in a controlled manner. The process also provides a surface with low contamination levels and is, therefore, suitable for studies investigating the influence of surface roughness on adhesion.

The fracture toughness of aluminium-epoxy adhesive joints showed a strong dependence on the angle of the surface profile introduced by the ultra-milling technique for very slow crack velocities in a high-humidity environment. If the surface roughness was considered as a ratio of the components of microscopic shear and peel this could be related to fracture energy through an exponential relationship.

The aluminium-epoxy joints prepared by ultra-milling all failed at the adhesive-oxide interface when stressed in a humid environment.

Failure under humid conditions produced smooth, featureless adhesive fracture faces. This contrasted with the cohesive fracture observed for dry failure. Here the fracture showed evidence of furrows and plastically-deformed adhesive. The change in adhesive fracture surface appearance suggests that some changes in the energy-dissipation processes occurring for humid fracture, relative to dry fracture, may be occurring.

Scanning Auger microscopy of the fracture surface of bonds prepared using ultra-milled adherends suggests that moisture diffusion ahead of the crack front in failed wedge samples is inhomogeneous. This is consistent with inhomogeneities in the distribution of interfacial voids formed under stress. There is mounting evidence leading to a model of interfacial water diffusion, facilitated by stress-induced cavities (or voids) in the adhesive ahead of the crack tip.

The extent of bond degradation caused by stress-induced moisture ingress ahead of the crack tip depends strongly on surface micro-topography. As the surface profile angle increases, the diffusion of water ahead of the crack front decreases. The dependence of moisture diffusion on surface micro-topography is the result of a complex interaction between stress and the micro-mechanics of the bond interphase region.

Acknowledgments

The authors would like to thank Dr. Chester, DSTO, and Dr. Underhill, The Royal Military College of Canada, for advice provided during the writing of the manuscript.

References

[1] Huntsberger, J. R., *Adhes. Age* **13**(11), 43 (1970).
[2] Keisler, C. and Lataillade, J. L., *J. Adhes. Sci. Technol.* **9**, 395 (1995).
[3] Chang, W. V., *J. Appl. Polym. Sci.* **26**, 1759 (1981).
[4] Arrowsmith, D. J., Moth, D. A. and Rose, S. P., *Int. J. Adhes. Adhes.* **12**, 67 (1992).
[5] Bhatt, B. D. and Radhakrishnan, V., *J. Adhes. Sci. Technol.* **3**, 383 (1989).
[6] Martinez, J. M., Fernandez-Garcia, J. C., Huerta, F. and Orgiles-Barcelo, A. C., *Rubber. Chem. and Technol.* **64**, 510 (1991).
[7] Jennings, C. W., *J. Adhes.* **4**, 25 (1972).
[8] Evans, J. R. and Packham, D. E., *J. Adhes.* **9**, 267 (1978).
[9] Evans, J. R. and Packham, D. E., *J. Adhes.* **10**, 39 (1979).
[10] Evans, J. R. and Packham, D. E., *J. Adhes.* **10**, 177 (1979).

[11] Packham, D. E., *Int. J. Adhes. Adhes.* **6**, 225 (1986).
[12] Sargent, J. P., *Int. J. Adhes. Adhes.* **14**, 21(1994).
[13] Zhang, Y. L. and Spinks, G. M., *J. Adhes. Sci. Technol.* **11**(2), 20 (1997).
[14] Briscoe, B. J. and Panesar, S. S., *J. Phys. D: Appl. Phys.* **25**, A20 (1992).
[15] Minford, J. D., In: *Treatise on Adhesion and Adhesives*, **5**, Patrick, R. L. Ed. (Marcel Dekker, New York, 1981), 69–76.
[16] Critchlow, G. W. and Brewis, D. M., *Int. J. Adhes. Adhes.* **16(4)**, 255 (1996).
[17] Olsson-Jacques, C. L., Wilson, A. R., Rider, A. N. and Arnott, D. R., *Surf. Interface Anal.* **24**, 569 (1996).
[18] Carré, A. and Schultz, J., *J. Adhes.* **20**, 1 (1986).
[19] Cognard, J., *J. Adhes.* **57**, 31 (1996).
[20] Marceau, J. A. and Thrall, E. W., In: *Adhesive Bonding of Aluminium Alloys*, Thrall, E. W. and Shannon, R. W. Ed., Chp. 10, pp. 177–197, Marcel Dekker, New York (1985).
[21] Stone, M. H. and Peet, T., *Royal Aircraft Establishment Technical Memorandum Mat 349*, July, 1980.
[22] Hardwick, D. A., Ahearn, J. S. and Venables, J. D., *J. Mater. Sci.* **19**, 223 (1984).
[23] Kinloch, A. J., *Adhesion and Adhesives* (Chapman and Hall, London, 1987), p. 270.
[24] Kinloch, A. J., Gilbert, D. G. and Shaw, S. J., *J. Mater. Sci.* **21**, 1051 (1986).
[25] Rider, A. N., Olsson-Jacques, C. L. and Arnott, D. R., *Surf. Interface Anal.* **27**, 1055 (1999).
[26] Lambrianidis, L. T., Arnott, D. R., Wilson, A. R., Vandenberg, J. and Vargas, O., *Proc. Intl. Aero. Cong.*, Melbourne, Australia, pp. 355–360 (1995).
[27] 1992 Annual Book of ASTM Standards, Section 15, Vol. 15.06, Adhesives.
[28] Arnott, D. R., Wilson, A. R., Rider, A. N., Lambrianidis, L. T. and Farr, N. G., *Appl. Surf. Sci.* **70/71**, 109 (1993).
[29] Tanuma, S., Powell, C. J. and Penn, D. R., *Surf. Interface Anal.* **11**, 577 (1988).
[30] Carré, A. and Schultz, J., *J. Adhes.* **15**, 151 (1983).
[31] Baker, A. A. and Chester, R. J., *Int. J. Adhes. Adhes.* **12**(2), 73 (1991).
[32] Chester, R. J., unpublished results.
[33] Baker, A. A., Chester, R. J., Davis, M. J., Roberts, J. D. and Retchford, J. A., *Composites* **24**(6) (1993).
[34] Chalkley, P., "*A Critical Compendium of Material Property Data for Bonded Composite Repairs*", DSTO-DDP-0274, p. 6, DSTO-AMRL, Melbourne (1997).
[35] Critchlow, G. W. and Brewis, D. M., *Int. J. Adhes. Adhes.* **15**(3), 255 (1995).
[36] Mantel, M. and Wightman, J. P., *Surf. Interface Anal.* **21**, 595 (1994).
[37] Pearce, P. J., Ennis, B. C., Grabovac, I. and Morris, C. E. M., *J. Adhes.* **47**, 123 (1994).
[38] Pearce, P. J., Ennis, B. C., Grabovac, I. and Morris, C. E. M., unpublished data.
[39] Sharon, G., Dodiuk, H. and Kenig, S., *J. Adhes.* **30**, 87 (1989).
[40] Arnott, D. R. and Kindermann, M. R., *J. Adhes.* **48**, 101 (1995).
[41] Comyn, J., In: *Durability of Structural Adhesives*, Kinloch, A. J. Ed., Applied Science, London, 1983, Chap. 3.
[42] Kim, R. H. and Broutman, L. J., *4th Int. Conf. Deformation, Yield and Fracture in Polymers*, Cambridge (1971).
[43] Minford, J. D., In: *Treatise on Adhesion and Adhesives*, **5**, Patrick, R. L. Ed. (Marcel Dekker, New York, 1981), 47–48.
[44] Plueddemann, E. P., *Silane Coupling Agents*, 2nd edn. (Plenum Press, New York, 1991).
[45] Patrick, R. L., "The use of SEM", In: *Treatise on Adhesion and Adhesives*, Vol. 3, Patrick, R. L. Ed. (Marcel Dekker, N.Y., 1973).
[46] Arnott, D. R., Rider, A. N., Wilson, A. R., Olsson-Jacques, C. L., Lambrianidis, L. T. and Pearce, P. J., "*Bond Durability Performance – The Australian Silane Surface Treatment*", *Congress of ICAS*, 13–18 September, 1998, Melbourne, Australia, *published conference proceedings.*